Directional and Single-Crystal Solidification of Ni-Base Superalloys: Part I. The Role of Curved Isotherms on Grain Selection

N. D'SOUZA, M.G. ARDAKANI, M. McLEAN, and B.A. SHOLLOCK

The development of crystallographic texture during directional solidification has been quantitatively analyzed in columnar castings of the Ni-base superalloys, CMSX4 and CM186LC, produced with a range of cooling rates and liquidus front curvatures. It is proposed that the more diffuse crystallographic texture developed in CMSX4 relative to CM186LC results from a combination of the differing local orientation stability condition and the alloys' solidification characteristics. The implications of these additional factors on the evolution of the axial grain texture, the grain orientations produced in single-crystal processing, and the stability of spurious grains in processing CMSX4 are discussed. An experimental method is presented to quantitatively analyze the grain selection process in the case of curved liquidus isotherms by retaining the stereology of the primary ⟨001⟩ dendrite growth direction and the local thermal gradient vector. This can account for the stability of spuriously nucleated edge grains in a single-crystal matrix.

I. INTRODUCTION

THE development of directional and single-crystal casting technology for the production of turbine blades has been a key factor in the evolution of the gas turbine for aerospace applications.[1] Versnyder and Shank[1] pioneered these closely related processes, which led to improved ductility, creep rupture, and thermal fatigue resistance. Walton and Chalmers[2] reported the existence of a preferred crystallographic orientation in columnar-grained castings produced in a positive thermal gradient and attributed this preferred orientation to anisotropic growth rates of dendrites associated with grains of different orientations. In cubic alloys, grains with ⟨001⟩ aligned parallel to the temperature gradient have the fastest growth rate and overgrow the slower growing orientations. This grain selection mechanism is of practical importance, since

(1) superalloy directional and single-crystal castings are invariably produced with a dendritic growth front morphology; and
(2) the natural ⟨001⟩ axial texture coincides with the direction of minimum Young's modulus leading to reduced thermal stresses and enhanced thermal fatigue resistance of gas turbine blades in service.

There have been several proposals of the factors controlling solidification texture. Walton and Chalmers[2] have suggested that the ⟨001⟩ fast growing directions in cubic crystals are a consequence of the anisotropy of the surface energy. Direct observations of ⟨001⟩ dendritic growth in the organic analogue, succinonitrile, by Huang and Glicksman[3] supported this conclusion. Goss[4] suggested that dendrites grow in the direction having the highest thermal conductivity; however, in cubic systems, such as superalloys, the thermal conductivity is isotropic.[5] Lee *et al.*[5] have investigated the fast growing directions in fcc (Al, Pb), bcc (Fe, Cr), hcp (Zn), and bct (Sn) systems, suggesting that the strain energy (thermal stresses) arising in the dendrite because of the orientation-dependent Young's modulus is also an important factor. It is proposed that the ⟨111⟩ dendritic growth in chromium, where the thermal conductivity is isotropic and the anisotropy of the surface energy criterion predicts the existence of the ⟨001⟩ fast growing direction, results from such thermal stresses.

Quested and McLean[6] have related the morphology of the growth front in directionally solidified (DS) superalloys to the G/V ratio and the scale of the dendrites to the solidification conditions. (G is the temperature gradient in the melt ahead of the solidifying front and V is the rate of solidification.) More recently, Gandin *et al.*[7,8] have characterized the evolution of grain orientations during the directional solidification of an INCONEL* alloy, showing that the sharp ⟨001⟩ axial texture produced is consistent with the competitive grain growth concept of Walton and Chalmers.[2]

Recent developments in single-crystal superalloy technology have focused on the following.

(1) The development of novel alloy compositions with increased temperature capability. The progressive increase in creep strength and maximum stress-bearing temperatures have been achieved by a combination of increases in the volume fraction and solvus temperature of the γ' precipitate and increasing concentrations of refractory solid solution strengthening elements (W, Mo, and Re). However, this improvement in mechanical performance has been accompanied by increasing difficulty in achieving and maintaining the optimum single-crystal orientation and structure. In particular, high pressure turbine blades produced from second generation superalloys such as CMSX4 in the commercial foundry using

---

*INCONEL is a trademark of INCO Alloys International, Inc., Huntington, WV.

N. D'SOUZA, Postdoctoral Research Assistant, M.G. ARDAKANI, Research Associate, M. McLEAN, Professor and Head of Department, and B.A. SHOLLOCK, Senior Lecturer, are with the Department of Materials, Imperial College of Science, Technology and Medicine, London SW7 2BP, United Kingdom.

Manuscript submitted October 19, 1999.

helical grain selectors show a much wider range of axial orientations of up to 18 deg.[9]

(2) Extension of single-crystal technology from small aerospace components to the much larger parts required for industrial gas turbines (IGT) for electricity generation. Scaling-up the process is not straightforward. The larger mass of the castings and their lower surface to volume ratio have a very direct effect on the heat-transfer characteristics of the process, leading to lower temperature gradients (G) at the solid-liquid interface. This, in turn, requires a lower solidification rate (V) in order to exceed the critical G/V ratio to prevent equiaxed solidification.[6] These lower values of G and V are likely to accentuate the intrinsic instabilities in an extended semisolid region. Also, in large IGT-scale castings, or in cluster molds of complex components (*e.g.*, nozzle guide vanes), there is much less control of the heat flow characteristics that can result in curved isotherms, which may increase the deviation of the final axial texture from ⟨001⟩ and produce conditions for freckling and spurious grain formation.[10]

It is manifest that much of the potential benefit of single-crystal castings will be lost if the specifications for crystal orientation and defect concentration are relaxed. The present investigation characterizes the grain structures and orientations produced during processing of two modern superalloys, CMSX4 and its DS derivative CM186LC, in conditions where the curvature of the liquidus isotherms was varied. The two principal objectives of the study are the following:

(1) to understand the role of the curved liquidus isotherms in the competitive grain growth process from the point of view of directional solidification and the stability of spurious grains in single-crystal processing; and
(2) to clarify the role of alloy constitution in altering the efficacy of the competitive grain growth process.

Columnar grain growth leading to the evolution of a crystallographic texture occurs in a number of metallurgical processes, *e.g.*, vacuum arc remelting (VAR). Where the solid-liquid interface is highly curved, as in VAR processes, the columnar grains generally grow normal to the local solidification front.[11,12] Indeed, from the inclination of the columnar grains across the specimen section, Ward *et al.*[13] have deduced the shape of the solidification front. The attainment of an axial texture during directional solidification has been the subject of investigations in a range of Ni-base superalloys. Directional solidification of IN750 and CMSX4 has been shown to result in an axial texture within 12 deg of ⟨001⟩.[8,9] It is therefore a matter of interest to ascertain the following:

(1) the extent to which the axial texture after a given solidification length is dictated by the local heat flux conditions at the solidification front; and
(2) the role that the dendrite tip morphology plays in the intrinsic dendritic growth process, which subsequently affects grain selection in the presence of a positive thermal gradient.

Both of these factors would be expected to have an influence on the competitive grain growth process. In this investigation, the role of curved liquidus isotherms will be studied.

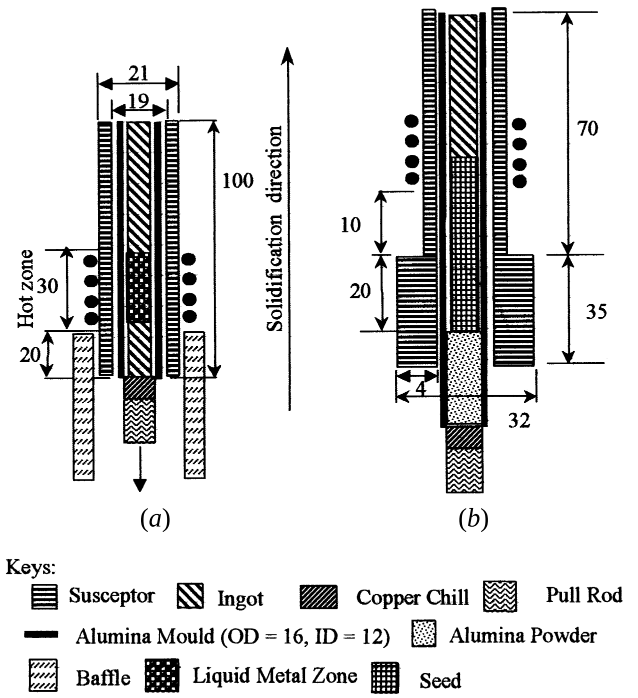

Fig. 1—Schematic diagrams of the solidification rigs used for (*a*) high thermal gradient directional solidification (experiments 1 through 5, Table I) and (*b*) low thermal gradient directional solidification (experiment 6, Table I) and single-crystal growth experiments (experiments 7 through 10, Table I). Dimensions are in millimeters.

II. EXPERIMENTAL METHODS

Directional and Single-Crystal Solidification

Directional and single-crystal SX solidification experiments encompassing a range of cooling rates were carried out using a Bridgman crystal growth apparatus (Figure 1) with Radio Frequency (RF) heating of precast ingots (≈12-mm diameter) using graphite susceptors in an atmosphere of flowing argon. An important aspect of this investigation is the quantitative analysis of the competitive grain growth mechanism at curved liquidus isotherms, which result from a radial component of the thermal gradient, in addition to the vertical component directed downward through the solid ingot to a water-cooled copper chill plate. Two methods were adopted to generate this radial component of the thermal gradient.

(1) Directional solidification was achieved by translation of a liquid metal zone of ~30-mm length along the length of the initial charge. Adjustment of the radiation baffles at the base of the hot zone, which also corresponds to the position of the solid-liquid interface, increased the radial component of heat flux from the solidified ingot. The experimental configuration, which is shown schematically in Figure 1(a) was used in experiments 1 through 5 in Table I. In these experiments, the charge was completely melted and allowed to be quenched at the chill plate to randomly nucleate grains; the texture was then allowed to develop along the length of the DS ingots.
(2) The vertical component of the thermal gradient was reduced by isolating the base of the ingot from the water-cooled chill with various thicknesses of alumina powder between the ingot and the chill plate. This was used in

Table I. Matrix of Directional and Single-Crystal Solidification Experiments

Experiment	Alloy	Nature of Ingot	$V \times 10^5$ (ms^{-1})	L (mm)	λ_P (μm)	G (K mm^{-1})
1	CMSX4	DS	1.9	0	185	10 ± 2
2	CMSX4	DS	4.1	0	165	11 ± 4
3	CMSX4	DS	6.2	0	160	13 ± 3
4	CM 186LC	DS	1.9	0	185	10 ± 2
5	CM 186LC	DS	6.2	0	177	10 ± 3
6	CMSX4	DS (initial)	3.0	80	302	3 ± 1
		DS (final)			275	3 ± 1
7	CMSX4	SX (initial)	3.0	20	315	3 ± 1
		SX (final)			286	3 ± 1
8	CMSX4	SX (initial)	3.0	40	315	3 ± 1
		SX (final)			293	3 ± 1
9	CMSX4	SX (initial)	1.9	80	295	4 ± 1
		SX (final)			267	5 ± 1
10	CMSX4	SX (initial)	4.1	80	272	3 ± 1
		SX (final)			227	6 ± 2

L = length of alumina powder, λ_P = primary dendrite spacing, and SX = single crystal.

experiments 6 through 10 in Table I. In experiments 7 through 10, seed single crystals were used to initiate single-crystal growth. Figure 1(b) shows the starting configuration of the single-crystal seed, graphite susceptor, recrystallized alumina mold, and external copper windings. A susceptor with a sharp change in thickness was used to further control the temperature gradient and ensure that only part of the single-crystal seed was melted. This configuration led to a range of thermal conditions along the length of the ingot. For the initial 15 mm of withdrawal, the lower portion of the mold could only radiate weakly to the hot susceptor, which in combination with insignificant vertical heat flux to the chill results in significantly curved isotherms. However, beyond a withdrawal length of 15 mm, the descending mold can radiate strongly to the cooler surroundings, leading to an increased vertical component of the heat flux at the growth front, which steadily acquires a more planar profile. During partial melt back, the overflow of liquid metal into the gap between seed crystal and mold led to nucleation of stray grains at edges of the casting, whose stability relative to the seed crystal during subsequent directional solidification was investigated.

The temperature gradient (G) in experiment 1 (Table I) was measured directly from thermocouples embedded in the material being DS. The value of G measured directly correlated well with that deduced from the primary arm spacing (λ_P). The relation $\lambda_P \propto G^{-1/2} \times V^{-1/4}$ derived by Hunt[14] has been shown by Quested and McLean[6] and more recently by Pollock and Murphy[15] to account for the variation of λ_P, with the solidification conditions for a range of superalloys. Moreover, the variation of λ_P with the product $G^{-1/2} \times V^{-1/4}$ for all superalloys considered to date fall on a common curve. The present results are fully consistent with this behavior. Consequently, λ_P has been taken as an indication of G for most of the ingots examined (Table I). The uncertainties in G due to errors in measurement of λ_P are indicated.

The solid-liquid interface shapes were determined for a range of solidification conditions using a tungsten (W) decoration technique. When the molten zone reaches the thin layer (~250 μm) of W powder that is placed between two segments of the alloy charge, they rapidly settle uniformly on the solid-liquid interface interrupting the continuation of dendritic growth (Figure 2(a)). The initial W particles were irregular in shape and had an average size in the range of 30 to 80 μm. A similar size distribution of the W particles residing on the dendrite tips along with an unaltered cruciform dendrite tip morphology (Figure 2(a)) suggests that W particles have not undergone significant dissolution, thereby indicating that the W addition has not altered the solidification conditions and the local G at the liquidus isotherm. Indeed, in VAR of an IN718 alloy, the melt pool shape was identified by observing dark regions of W by a macroscopic examination of longitudinal sections through the ingot. In this case, good agreement between the experimentally determined melt pool shape and that determined by grain orientation measurements suggested that the W additions did not affect the alloy solidification conditions.[13] Figures 2(b) and (c) show photographs of such W decorated surfaces with low and high curvatures, respectively (curvature is defined as 1/R), and Figure 2(d) shows the curvature on a longitudinal portion of the interrupted ingot. The shape of the solid-liquid interface approximates to a spherical surface. The curvature of the solid-liquid surface can be calculated from the vertical distance between the perimeter and the central portion of the curved surface and the radius of the ingot. The relation of the surface inclinations at various portions on the transverse section to the local curvature is given in the Appendix.

Specimens were prepared for metallographic and grain orientation characterization by mechanical and electropolishing to remove any surface deformed layers produced during preliminary cutting, grinding, and polishing. These samples were examined by means of the electron back scattered diffraction technique in a JEOL* 840 scanning electron microscope, equipped with SINTEF hardware and CHANNEL + software for automatic grain indexing and mapping. The samples were tilted so that the angle between the electron beam and the surface normal was 70 deg. The surface was scanned using an average incremental step size of 20

---

*JEOL is a trademark of Japan Electron Optics Ltd., Tokyo.

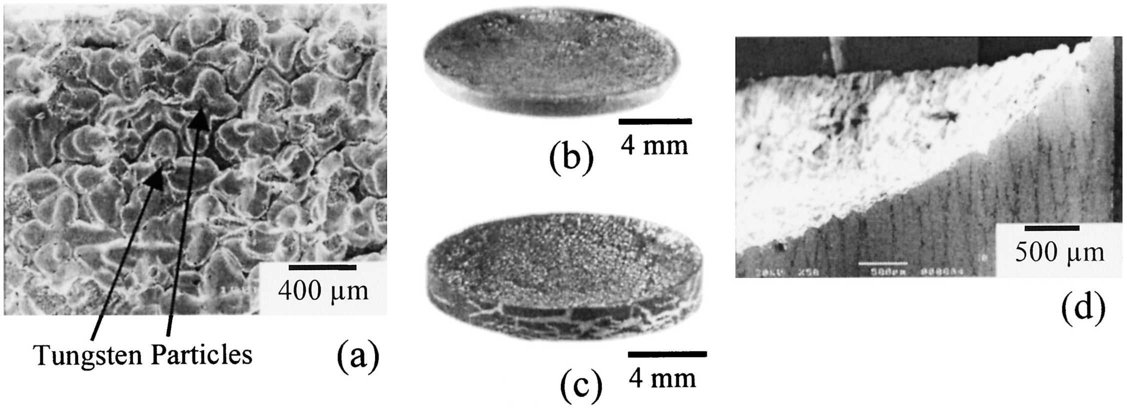

Fig. 2—(*a*) Tungsten particles on dendrite tips on the interrupted solidification surface; (*b*) and (*c*) specimen sections showing interfaces of low and high curvatures, respectively; and (*d*) secondary electron image showing a longitudinal section of (c).

to 100 μm depending on the grain size, so that at least 25 to 50 (sampling) grid points were analyzed per grain. All of the grain orientations were specified with respect to a coordinate system based on the ingot geometry; the *Z*-axis was parallel to the macroscopic growth, and the *X* and *Y* axes were parallel to arbitrary, orthogonal transverse directions that were identified on the grain maps that were constructed to show the spatial location of grains on a given section. In addition to the specimen reference axes described previously, the other reference axes are the three orthogonal crystal axes, or the three $\langle 001 \rangle$ directions. In the case of a transverse section, therefore, with respect to the specimen and crystal reference axes, from the definition of the Euler angle rotations, the second Euler angle (Φ) represents the deviation of the primary $\langle 001 \rangle$ dendrites from the macroscopic growth axis[16] (Appendix). The grain orientations were displayed as $\{001\}$ pole figures (PFs) and inverse pole figures (IPFs).

The compositions of the Ni-based superalloys, CMSX4 and CM186LC, used in this study are listed in Table II.

III. RESULTS

A. *Development of Columnar Grain Texture during Directional Solidification*

1. *Effects of interface curvature and solidification length*

The montage in Figure 3 shows longitudinal sections of an ingot of CMSX4 directionally solidified at 1.9×10^{-5} ms^{-1} in conditions that produced a solid/liquid interface with a distinct curvature (experiment 1, Tables I and III). The IPFs showing orientations of grains at different distances from the ingot base are also shown. As solidification proceeds, there are two distinct trends.

(1) The number of grains progressively decreases and their morphology develops from being equiaxed to being

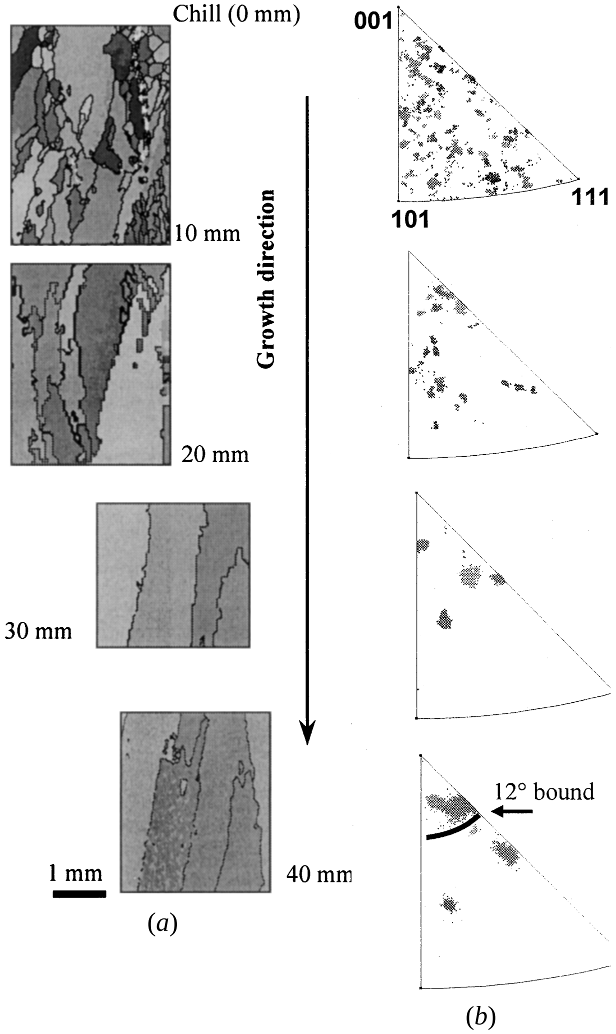

Fig. 3—(*a*) Grain maps along longitudinal sections and (*b*) inverse pole figures at different distances along an ingot of CMSX4 DS at 1.9×10^{-5} ms^{-1} in a temperature gradient of 10 K mm^{-1} (experiment 1, Table I).

Table II. Alloy Composition

Alloy	Cr	Co	Mo	W	Ta	Re	Al	Ti	Hf	Ni	C	T_L °C	T_S °C
CMSX4	6.5	9	0.6	6	6.5	3	5.6	1.0	0.1	bal	0.00	1387	1347
CM186LC	6.0	9	0.5	8	3.0	3	5.7	0.7	1.4	bal	0.07	1380	1320

Table III. Shape of Solid-Liquid Interlace for Selected Solidification Conditions

Experiment	L (mm)	H (mm)	LS (mm)	R (mm)	$\Psi_{\max}$ (Deg)
1	0	0.64	40	28	12
7	20	1.79	30	19	25
7	20	1.07	55	30	15
6, 9, 10	80	2.60	30	14	36
6, 9, 10	80	1.07	50	30	15

L = length of alumina powder, H = height difference across solid - liquid interface, LS = length of ingot solidified, R = radius of curvature, and $\Psi_{\max}$ = maximum interface inclination.

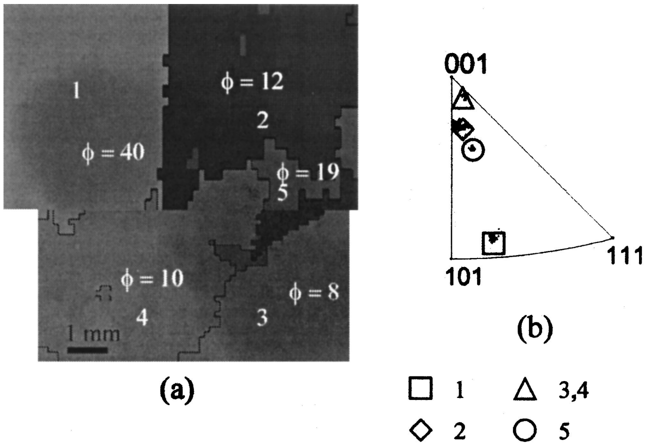

Fig. 4—(*a*) and (*b*) Grain map of a transverse section and corresponding inverse pole figure at 60 mm from the start of directional solidification at 3×10^{-5} ms^{-1} in a temperature gradient of 3 K mm^{-1} (experiment 6, Table I).

columnar with the long grain axis being parallel to the ingot withdrawal direction.

(2) The orientations in the initial quenched alloy are essentially random. As the columnar grains develop, a few grain orientations persist. These cluster around the ⟨001⟩ pole but deviate significantly from it, although there were grains in the original quench zone that were oriented with ⟨001⟩ closely aligned with the macroscopic growth direction.

The maximum interface inclination to the macroscopic direction of solidification $\Psi_{\max}$, measured by the W decoration technique for each condition, is listed in Table III. For the particular case of experiment 1, $\Psi_{\max}$ is about 12 deg. It is noteworthy that most grains in the DS ingot produced in experiment 1 have primary ⟨001⟩ orientations within 15 deg of the macroscopic direction of solidification (Φ) after a solidification length of 40 mm.

The influence of the curved liquidus isotherms on the grain selection leading to texture evolution is further exemplified by experiment 6. By isolating the ingot from the water-cooled hearth, the initial stage of solidification had little longitudinal heat loss leading to a value of Φ of about 36 deg (Table III). As directional solidification proceeds, radiation from the solidified ingot to cool surroundings enhances longitudinal heat loss and reduces the interface curvature so that $\Psi_{\max}$ decreases to about 15 deg. Figure 4 shows an IPF indicating the range of orientations after solidification of 60 mm. Grains with ⟨001⟩ deviating by up to 40 deg from the macroscopic solidification direction that were generated in the early stage of directional solidification have persisted. In this case, only the final transverse section has been shown, rather than the montage as in Figure 3, since in both cases directional solidification is initiated by the melting of the ingot base, producing a random grain orientation distribution.

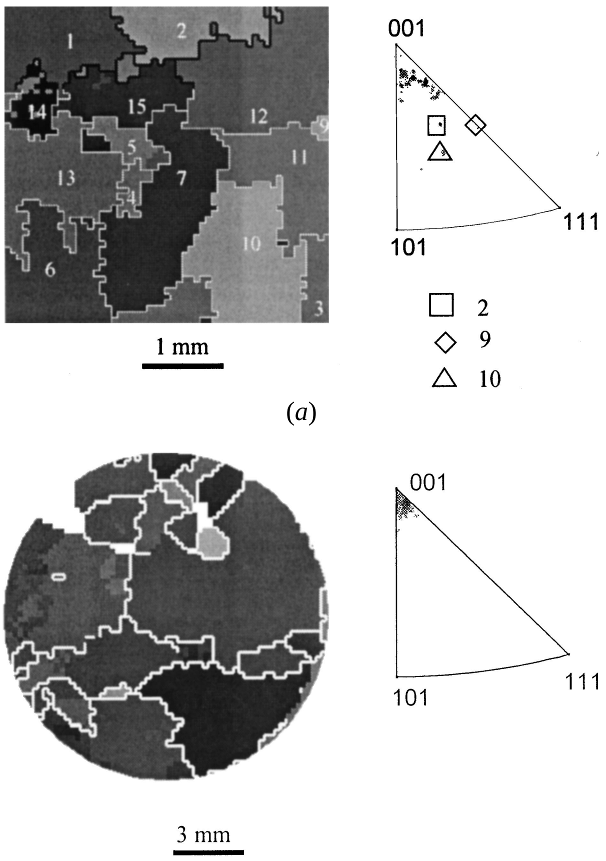

(*a*)

(*b*)

Fig. 5—(*a*) and (*b*) Grain map and accompanying inverse pole figure of a transverse section for CMSX4 corresponding to a directional solidification length of 40 mm at 1.9×10^{-5} ms^{-1} in a temperature gradient of 10 K mm^{-1}; (b) CM186LC (experiments 1 and 4, Table I).

2. *Different alloy behavior*

The grain orientations in CMSX4 and CM186LC, solidified under similar conditions at a solidification rate of 1.9 $\times$ 10^{-5} ms^{-1} (experiments 1 and 4, Table I), have been compared. Figure 5(a) shows a representative area from a transverse section of CMSX4 after a solidification length of 40 mm together with the IPF showing the grain orientations for the entire section. Figure 5(b) corresponds to CM186LC solidified in similar conditions to CMSX4. In both cases, directional solidification was initiated by the random nucleation of grains where the molten alloy contacted the water-cooled copper chill, resulting in a similar grain size distribution and random axial orientations encountered for both alloys.

Despite the similar solidification conditions, there are two distinct differences between the two IPFs.

(1) the deviation of the axial orientations from ⟨001⟩ is much

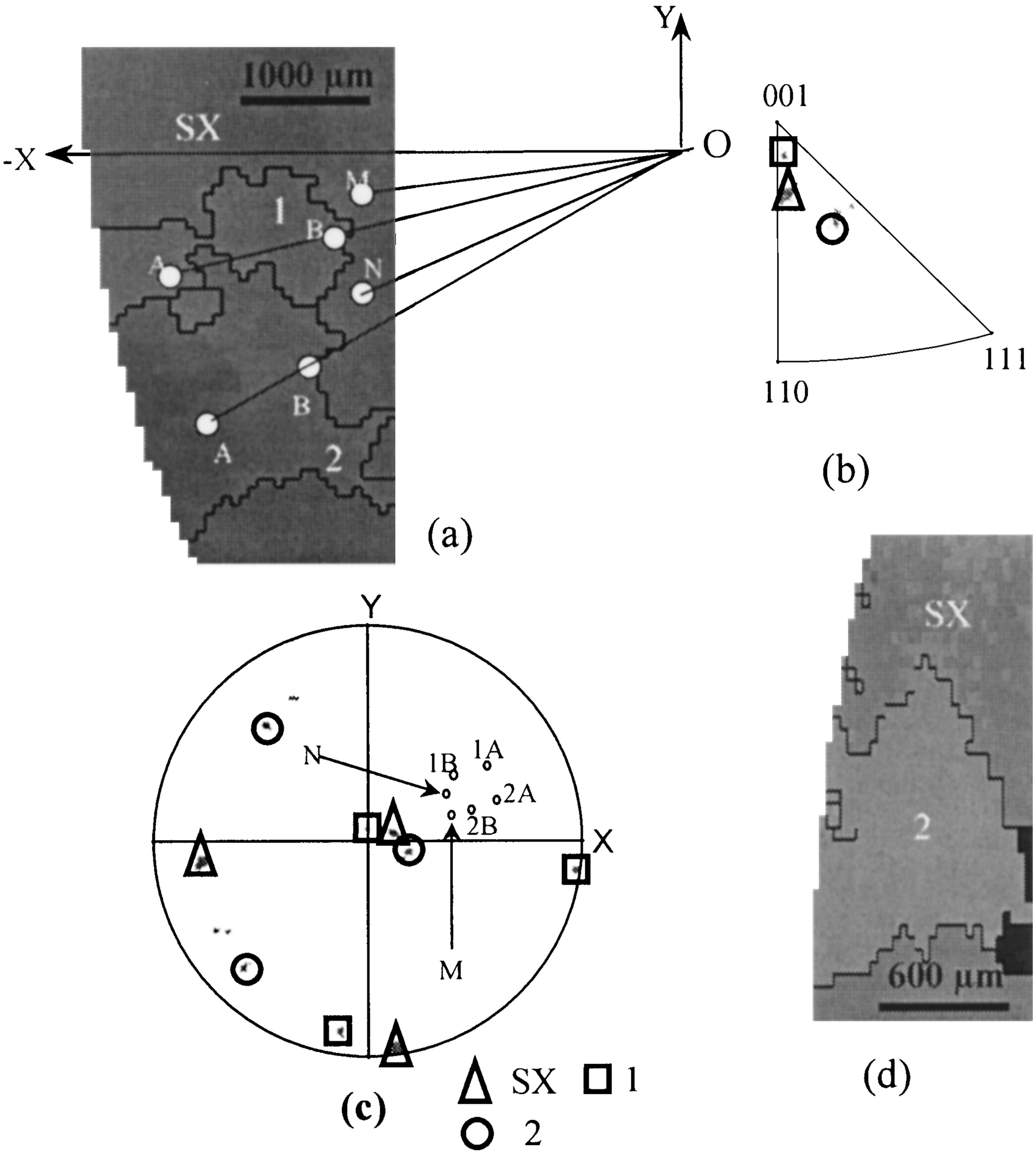

Fig. 6—(*a*) Grain map of CMSX4 single-crystal growth showing matrix and spurious edge grains on a transverse section (experiment 9, Table I). (*b*) Inverse pole figure and (*c*) {001} pole figure for grains in (a). (*d*) Grain map after further 10 mm of crystal growth.

greater for CMSX4 (up to 15 deg) than of or CM186LC (within 8 deg).

(2) A decreased grain density is apparent in the case of CM186LC. In CMSX4, grains with ⟨001⟩ significantly deviating from the ingot axis continue to grow after 40 mm of directional solidification.

B. *Stability of Spurious Grains during Single-Crystal Growth*

During growth of a single crystal of CMSX4 from a seed, spurious edge grains were formed where molten metal flowed down the mold/seed gap and solidified. The competitive growth of the seed orientation and the nucleated grains along the ingot length during directional solidification has been investigated under a number of solidification conditions that lead to quite different curvatures of the solid/liquid interface. Because there are few grains in a transverse section, it is possible to fully characterize the grain orientations in relation to the local inclination of the solid/liquid interface.

Figure 6(a) shows a transverse section of a seeded single crystal in which two spurious grains have nucleated at the edge of the single crystal (experiment 9, Table I). Grain 1 has a near ⟨001⟩ axial orientation with $\Phi = 7$ deg (Figure 6(b)), while grain 2 and the seed crystal orientations are more remote from ⟨00l⟩ ($\Phi = 22$ and 14 deg, respectively). The axial orientation of the as-received seed crystal deviated from ⟨001⟩ by 14 deg. Part of a transverse section corresponding to a further solidification length of 10 mm (Figure 6(d)) shows the overgrowth of grain 1, despite it having a

Table IV. Deviation of the ⟨001⟩ Poles Nearest the Growth Axis of CMSX4 from the Local Thermal Gradient at Two Positions of the Growth Front 40 mm Apart (Experiment 9, Table I)

Grain (Position)	Figure	Φ°	Ψ_i°	$\angle^G_{\langle 001\rangle i^\circ}$	Ψ_{40}°	$\angle^G_{\langle 001@40^\circ}$
1 (A)	6(a)	7	34	33	14	overgrown
1 (B)	6(a)	7	31	28	11	overgrown
M (SX)	6(a)	14	36	16	11	prevails
2 (A)	6(a)	22	29	22	15	10*
2 (B)	6(a)	22	34	20	14	10*
N (SX)	6(a)	14	31	24	13	4*
3 (A)	7(a)	26	36	52	15	overgrown
3 (B)	7(a)	26	33	47	14	overgrown
S (SX)	7(a)	14	31	36	13	prevails
4 (A)	7(a)	44	36	20	15	30 overgrown
4 (B)	7(a)	44	31	20	13	34 overgrown
R (SX)	7(a)	14	29	36	12	prevails
5 (A)	7(a) and (d)	26	36 (7(a))	36 (7(a))	14 (7(d))	22 (7(d))
5 (B)	7(a) and (d)	26	33 (7(a))	36 (7(a))	12 (7(d))	24 (7(d))
Q (SX)	7(a) and (d)	14	31 (7(a))	42 (7(a))	11 (7(d))	24 (7(d))
6 (A)	7(a)	18	36 (7(a))	38 (7(a))	15 (7(d))	28 (7(d))
6 (B)	7(a)	18	34 (7(a))	38 (7(a))	13 (7(d))	25 (7(d))
P (SX)	7(a) and (d)	14	32 (7(a))	42 (7(a))	12 (7(d))	24 (7(d))

Ψ_i° = at initial solidification front, $\angle^G_{\langle 001\rangle i^\circ}$ = at initial solidification front, Ψ_{40}° = after 40-mm solidification, and $\angle^G_{\langle 001\rangle 40^\circ}$ = after 40-mm solidification. * The relevant grain map has been omitted, being similar in nature to Fig. 6(d).

near ⟨001⟩ axial orientation, and the persistence of grain 2, which is oriented with ⟨001⟩ far from the macroscopic growth axis. The full (001) pole figure shown in Figure 6(c) identifies the surface normals to the solid-liquid interface at positions where the spurious grains occur. (These are indicated by A, B, M, and N). The deviation of the local normals from ⟨001⟩, designated $\angle^G_{\langle 001\rangle}$, are tabulated in Table IV. This shows that locally grain 2 and SX have similar misorientations from ⟨001⟩ that are both less than $\angle^G_{\langle 001\rangle}$ for grain 1. Figure 7(a) shows the stray edge grains 3, 4, 5, and 6 nucleated on another portion of the transverse section of Figure 6(a) (experiment 9, Table I). The corresponding IPF is shown in Figure 7(b). A transverse section after a solidification length of 10 mm (Figure 7(c)) shows the overgrowth of grain 3. However, within the given solidification length,

(1) the length of boundary between grains 4 and 5 increases (Figure 7(c)), and
(2) a boundary between grains 4 and 6 is formed (Figure 7(c)).

This can only occur if within the 10-mm solidification length, the consumption of the single-crystal matrix by grain 4 occurred. Taking account of the inclination of the solid-liquid interface confirms that the stable growth correlates with a relatively low value of $\angle^G_{\langle 001\rangle}$, as shown in Table IV, rather than the angle between the macroscopic growth axis and the orientation of the primary ⟨001⟩ dendrite ($\Phi = 44$ deg for grain 4). However, beyond a solidification length of 10 mm, grain 4 is overgrown by grain 5 and the single crystal. At this height (40 mm), the solidification conditions have progressively changed to increase the radius of curvature of the solid-liquid interface. Recalculating the values of $\angle^G_{\langle 001\rangle}$ for the shallower solid-liquid interface (Table IV) shows that grains 5, 6, and single crystal have similar values, while grain 4 has a much larger deviation of ⟨001⟩ from the local surface normal.

IV. DISCUSSION

A. *Role of the Curvature of the Liquidus Isotherms in Competitive Grain Growth*

The practice of directional solidification and single-crystal processing makes use of baffles and radiation shields to ensure that the solid-liquid interface is relatively planar. Under these conditions, the competitive grain growth mechanism of Walton and Chalmers[2] has been very successful in accounting for the orientations produced during directional solidification of superalloys. However, in the present experiments, where curved solid-liquid interfaces have been deliberately generated, stereological considerations associated with three-dimensional grain orientations and local thermal gradient vectors have to be addressed while quantifying the competitive grain selection process.

In CMSX4, the overgrowth of the near ⟨001⟩ axial orientations (grain 1, Figures 6(a) and (d)) and the remarkable stability of significantly off ⟨001⟩ axial orientations (grain 4, Figures 7(a) and (c)) are apparently not consistent with the classical grain selection process in which orientations are related to the macroscopic direction of solidification, as would be the case for planar isotherms.[2] However, when the grain orientations are related to the local normals to the solid-liquid interface, through the angle $\angle^G_{\langle 001\rangle}$, it is clear that stable grain growth generally occurs where there is a small local deviation of ⟨001⟩ from the surface normal (*i.e.*, when $\angle^G_{\langle 001\rangle}$ is small). In the special case of planar isotherms, the thermal gradient is uniaxial and normal to the ingot cross section and the angles $\angle^G_{\langle 001\rangle}$ and Φ are identical. It follows therefore that an exact ⟨001⟩ axial texture is to be expected only in the case of planar liquidus isotherms; for curved interfaces, there will be a range of orientations that are locally stable. Gandin *et al.*[8] have also reported that the final axial texture attained during the directional solidification of the INX750 superalloy was within 12 deg of ⟨001⟩, even

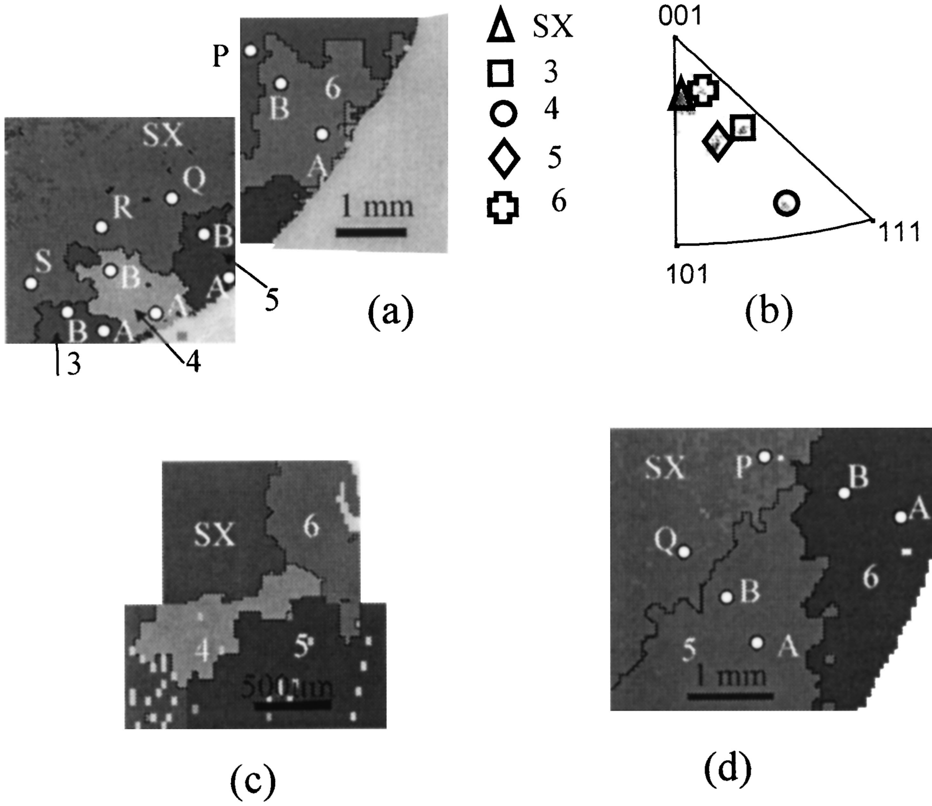

Fig. 7—(*a*) As Fig. 6(a) (experiment 1, Table I). (*b*) Inverse pole figure for transverse section shown in (a). (*c*) Grain map for transverse section 10 mm from (a). (*d*) Grain map for transverse section 40 mm from (a).

though they make the assumption of planar liquidus isotherms. They have attributed this scatter to a compromise between the probability of nucleating a grain with a ⟨001⟩ axial orientation ($\propto \sin \Phi$, for $0 \leq \Phi \leq \pi/4$) and the grain selection process that eliminates the larger misorientations. However, in the present investigation, we have found that the larger the deviation of the local solid-liquid interface from planarity, the larger will be the range of orientations that can occur in the DS texture (IPF in Figure 4). In broad terms, a planar solidification front leads to a sharp ⟨001⟩ texture; a curved solidification front will lead to a diffuse texture.

B. *Differences in Textures of CMSX4 and CM186LC*

CMSX4 and CM186LC have very similar chemistries and physical properties. In particular, the factors that will control heat flow are almost identical. Consequently, the same solidification conditions are likely to lead to similar profiles of the solid-liquid interface during solidification. However, quite different textures are produced in the two alloys; a sharp ⟨001⟩ texture in CM186LC and a very diffuse texture in CMSX4.

More detailed inspection of the orientations of grains in a transverse section of DS CMSX4 produced in experiment 1 shows that grains with ⟨001⟩ deviating significantly from the macroscopic axial direction are not restricted to the edges of the ingot where Ψ is relatively large. In the central region of the ingot cross section (Figure 5(a)), where the isotherms were nearly planar ($0 < \psi < 6$ deg), an exact ⟨001⟩ axial texture was absent and there was an average deviation of about 15 deg. Moreover, the presence of a few unfavourably oriented grains (2, 9, and 10) with $\angle^{G}_{\langle 001 \rangle} \approx 25$ to 35 deg suggest that orientations that are stable at the ingot perimeter can extend and persist in the center of the casting in the case of CMSX4 but not in CM186LC.

It has been shown that dendritic growth occurs far from the limit of constitutional undercooling.[6] In the case of directional solidification, when the dendrite tips are advancing into a positive thermal gradient, the tips of the dendrites favorably oriented with respect to the local G lead the tips of the unfavorably oriented dendrites, and the thermal and solute fields of the leading dendrites subsequently retard the growth of their neighbors.[2] This leads to overgrowth by rapid development of (010) and (001) secondary dendrite arms normal to the solidification direction and of (001) tertiary dendrites branching from these secondaries parallel to the solidification direction.[2] Consequently, dendrites stabilized at the edge of the casting will extend through the semisolid region into the melt and continue to grow in competition with other dendrites emanating from different parts of the solid-liquid interface. The distance over which edge grains are likely to propagate will be related to the dendrite length and the value of Ψ. The dendrite length L_d is simply related to the alloy melting range T_m and the temperature gradient at the solid-liquid interface G: $L_d = (T_m/G)$. For typical solidification conditions used in this study, the dendrites in CMSX4 and CM186LC have lengths up to 10 to 15 mm and can extend to the centers of the castings considered here. A comparison of the competitive grain selection process in CMSX4 and CM186LC is valid, since in both cases, the starting grain orientation distribution and grain

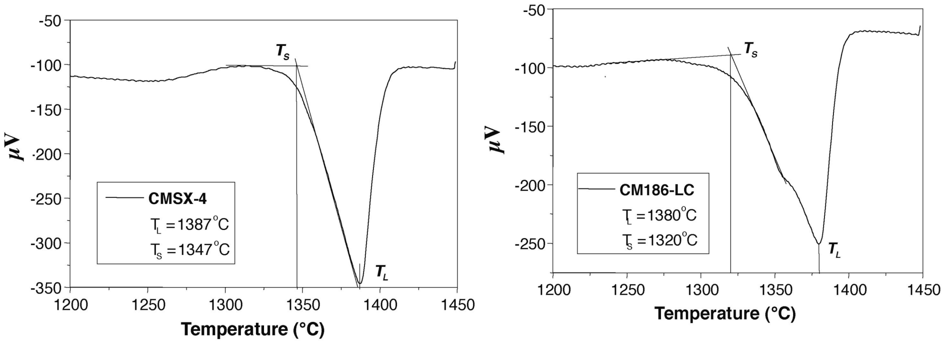

Fig. 8—DTA curves for CMSX4 and CM186LC showing liquidus, solidus, and carbide formation temperature.

densities are equivalent. This arises, since the chill zone that initiates grain selection leads to a random grain orientation distribution and an equiaxed grain morphology. Therefore, the observation in Section III–A–2 must reflect a more efficient grain selection mechanism by which dendrites of favored orientation overgrow the misoriented dendrites in the case of CM186LC than in CMSX4, under similar thermal environments. Differential thermal analysis (DTA) curves (Figure 8) show the alloy melting range for both alloys. The kink in the DTA curve for CM186LC, which is likely due to MC carbide formation is well below the liquidus temperature, and from the average G reported in Table I, the carbides are formed at least 1 mm behind the dendrite tip. We speculate that the nucleation and growth of secondary and tertiary dendrites required to achieve overgrowth is more rapid in the high fluidity of the carbon- and hafnium-rich interdendritic liquid of CM186LC than in CMSX4. Further work is required to clarify this issue.

C. *Some Processing Implications*

1. *Spurious grain growth during single-crystal casting*

The most damaging defects, which lead to casting rejection, are spurious grains. The present experiments have clearly shown that for stable growth, the grain must exhibit comparable or better stability than the matrix crystal with respect to competitive grain growth. It is not possible to specify a spurious grain orientation that will grow; rather, it is the orientation in relation to the inclination of the local solid-liquid interface that is important. The values of $\angle^{G}_{\langle 001\rangle}$ must be at least comparable for the matrix and stray crystal. Clearly, the curvature of the solid-liquid interface is important in determining which grains will persist during crystal growth, as was demonstrated previously in the experiments in which the interface curvature changed. However, the extent to which edge grains will grow toward the center of the casting and, consequently, be more damaging, is alloy specific.

2. *Implications for single-crystal casting technology*

If single-crystal turbine blades are to be produced with the natural $\langle 001\rangle$ axial orientation, it is important to control the range of axial orientations in the DS starter block. The range of single-crystal orientations produced is governed by the sharpness of the $\langle 001\rangle$ texture produced in the starter plate prior to use of a grain selector. In alloys giving a small range of orientations in the DS starter block, as in CM186LC, the central zone of the DS stub will be sharply $\langle 001\rangle$ so that a centrally placed grain selector will ensure that single crystals close to $\langle 001\rangle$ are produced. However, in alloys such as CMSX4, a diffuse texture pervades the entire DS structure leading to a wide range of single-crystal orientations. Since the combination of high levels of refractory solid-solution strengthening additions and low carbon content, characteristic of modern single-crystal alloy development, reduces the efficiency of grain overgrowth, it is inevitable that orientation control will become increasingly difficult.

V. CONCLUSIONS

1. The range of orientations produced during directional solidification of CMSX4 and CM186LC increases with increasing curvature of the solid-liquid interface. A wider range of axial orientations develops during the directional solidification of the alloy CMSX4 than in the case of its DS derivative, CM186LC.
2. The stability of spurious grains during single-crystal processing of CMSX4 can be related to the parameter $\angle^{G}_{\langle 001\rangle}$, which defines the deviation of $\langle 001\rangle$ from the local surface normal.
3. It is proposed that minor differences in alloy composition significantly alter the interdendritic liquid composition, which reduces the efficiency of secondary and tertiary dendrite development in CMSX4, allowing edge-stabilized grains to extend throughout the casting.

APPENDIX

Figure 9(a) is a schematic diagram showing two transverse sections (gray) along the length of the ingot and the corresponding profile of the liquidus surface, which is approximated by a spherical cap. In the two-dimensional sketch, the liquidus curve intersects the two transverse sections at points C and D. It is required to determine the orientation of the local thermal gradient vectors **CA** and **DA** with respect to a reference coordinate system. The specimen reference coordinate system comprises the macroscopic growth axis (Z) normal to the transverse section and two arbitrary orthogonal axes (X, Y) in the plane of the transverse section (Figure 9(a)). The following terms are used in the analysis.

The term R = the radius of curvature of the liquidus surface; (r, θ) = radial and angular coordinates on a transverse section; a = ingot radius; h and H = vertical distances from C and D, respectively, from the center of the liquidus

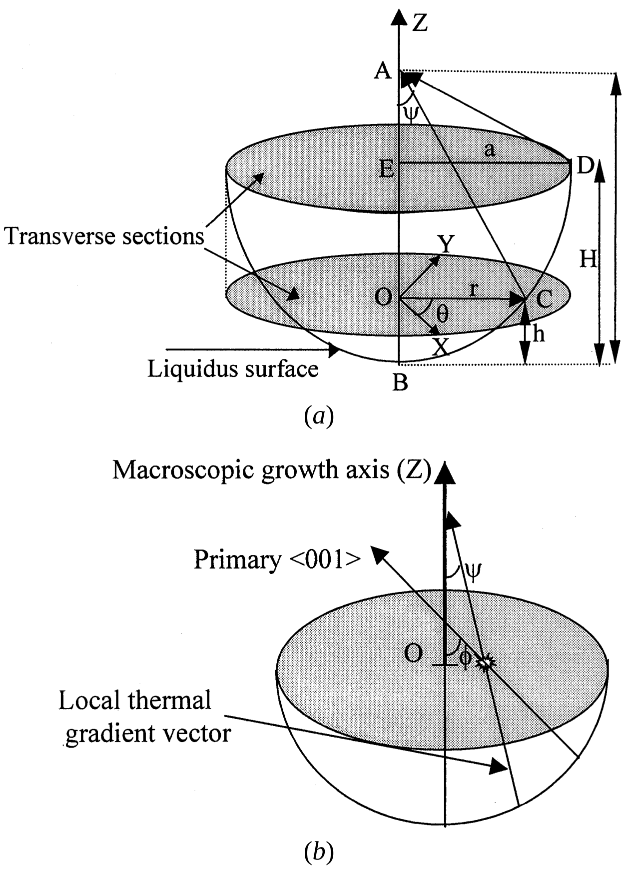

Fig. 9—(*a*) and (*b*) Schematic diagrams used for calculating the misorientation of the primary $\langle 001\rangle$ pole from the local thermal gradient (G) at a specific position on the transverse section.

surface (point B); and Ψ = inclination of the local thermal gradient vector, **G**, with the ingot axis.

Using the origin O, the coordinates of points A through D can be written as follows:

$$A = [0, 0, (R - h)] \qquad B = [0, 0, -h]$$

$$C = [r\cos\theta, r\sin\theta, 0] \; D = [a\cos\theta, a\sin\theta, (H - h)]$$

Since $\angle$AOC is a right angle:

$$(R - h)^2 + r^2 = R^2, \text{ which leads to } h = R - \sqrt{R^2 - r^2}, \text{ since } h < R \qquad [1]$$

$$\tan\Psi = \frac{r}{R - h} = \frac{r}{\sqrt{R^2 - r^2}} \qquad [2]$$

Since $\angle$AED is a right angle:

$$(R - H)^2 + a^2 = R^2, \text{ which leads to } R = \frac{a^2 + H^2}{2H} \qquad [3]$$

From Eq. [2], $\Psi = \Psi_{\max}$ when $r = a$. Therefore, from Eqs. [2] and [3]:

$$\tan\Psi_{\max} = \frac{a}{\sqrt{R^2 - a^2}} = \frac{2aH}{\sqrt{a^2 - H^2}} \qquad [4]$$

From the right angled ΔAOC:

$$R - h = R\cos\psi \text{ and } r = R\sin\psi \qquad [5]$$

The local thermal gradient vector (**CA**) can then be written as follows:

$$\mathbf{CA} = -r[\cos\theta\hat{i} + \sin\theta\hat{j}] + (R - h)\hat{k} \qquad [6]$$

The direction cosines (DCs) can therefore be expressed as follows:

$$\cos\alpha_1 = \frac{-r\cos\theta}{\sqrt{r^2 + (R - h)^2}} = \frac{-r\cos\theta}{R} = -\cos\theta\sin\Psi$$

$$\cos\alpha_2 = \frac{-r\sin\theta}{\sqrt{r^2 + (R - h)^2}} = \frac{-r\sin\theta}{R} = -\sin\theta\sin\Psi$$

$$\cos\alpha_3 = \frac{(R - h)}{\sqrt{r^2 + (R - h)^2}} = \frac{R\cos\Psi}{R} = \cos\Psi \qquad [7]$$

The DCs of the local thermal gradient vector **DA** can be obtained from Eq. [7] by putting $r = a$ and $\Psi = \Psi_{\max}$.

It is required to determine the angle between the local normal to the surface and the primary $\langle 001\rangle$ pole (Figure 9(b)). The $\{001\}$ pole figure displays the orientation of the three $\langle 001\rangle$ poles with respect to the specimen reference axis, from which the primary $\langle 001\rangle$ pole can be identified. From the values of the DCs with respect to the same specimen reference axes, the local G can be plotted on the same PF. Subsequently, the required misorientation between the local G and the primary $\langle 001\rangle$ pole can be determined from a Wulff net.

ACKNOWLEDGMENTS

The authors thank ALSTOM ENERGY (formerly European Gas Turbines) for provision of a studentship (ND'S) and EPSRC for support (Grant No. GR/L05433).

REFERENCES

1. F.L. Versnyder and M.E. Shank: *Mater. Sci. Eng.*, 1970, vol. 6, pp. 213-47.
2. D. Walton and B. Chalmers: *Trans. TMS-AIME*, 1959, vol. 215, pp. 447-56.
3. S.-C. Huang and M.E. Glicksman: *Acta Metall.*, 1981, vol. 29, pp. 701-15.
4. A.J. Goss: *Proc. Phys. Soc.*, 1953, vol. B116, pp. 525-32.
5. D.N. Lee, K.-H. Kim, Y. Lee, and C.-H. Choi: *Mater. Chem. Phys.*, 1997, vol. 47, pp. 154-58.
6. P.N. Quested and M. McLean: *Mater. Sci. Eng.*, 1984, vol. 65, pp. 171-80.
7. C.-A. Gandin and M. Rappaz: in *Materials Processing in the Computer Age—2*, V. Voller, S.P. Marsh, and N. El-Kaddah, eds., TMS, Warrendale, PA, 1995, pp. 117-28.
8. C.-A. Gandin, M. Rappaz, D. West, and B.L. Adams: *Metall. Mater. Trans. A*, 1995, vol. 26A, pp. 1543-52.
9. P. Carter, D.C. Cox, C.-A. Gandin, and R.C. Reed: *Mater. Sci. Eng. A*, 2000, vol. 280, pp. 233-46.
10. A. Mitchell: *Proc. Materials Engineering in Turbines and Compressors*, Charles Parson's Turbine Conf., A. Strang, ed., Institute of Materials, Newcastle, 1995, pp. 547-55.
11. X. Xu, R.C. Atwood, S. Sridhar, P.D. Lee, B. Drummings, R.M. Ward, and M. H. Jacobs: *Int. Symp. on Liquid Metal Processing and Casting*, A. Mitchell, L. Ridgeway, and M. Baldwin, eds., American Vacuum Society, Santa Fe, 1999, NM, pp. 76-89.
12. L. Nastac, S. Sunderraj, K.-O. Yu, and Y. Pang: *J. Met.*, 1998, pp. 30-35.
13. R.M. Ward, T.P. Johnson, and M.H. Jacobs: *Int. Symp. on Liquid Metal Processing and Casting*, A. Mitchell and P. Auburtin, eds., American Vacuum Society, Santa Fe, NM, 1997, pp. 97-109.
14. J.D. Hunt: *Solidification and Casting of Metals*, The Metals Society, London, 1979, pp. 3-9.
15. T.M. Pollock and W.H. Murphy: *Metall. Mater. Trans. A*, 1996, vol. 27A, pp. 1081-94.
16. V. Randle: *Microtexture Determination and Its Applications*, The Institute of Materials, London, 1992, p. 82.